Funded by the Horizon 2020 Framework Programme of the European Union

Grant Agreement nr.: 687008

Project acronym: GOTSolar

Project full title: New technological advances for the third generation of Solar cells

Deliverable D4.2 – Alternative metal oxide scaffold to TiO_2 to obtain device V_{oc} of 1.15V (Public Report)

Start date of the project: 01/01/2016	**Project coordinator name**: Adélio Mendes
Duration of the project: 36 months	**Institution of the Project coordinator:** UPORTO
Period covered by this report: from 01/01/2016 to 31/12/2016	**WP Reference**: WP4
Nr. pages: 16	**WP leader name:** Michael Grätzel
	Institution of the WP leader: EPFL

Funded by the Horizon 2020 Framework Programme of the European Union

Contents

Deliverable description 3
Summary 3
Introduction 4
Materials and methods 5
Substrate preparation and Li-doping TiO_2 5
DSSC preparation procedure 5
Perovskite precursor solution and film preparation 5
Hole transporting layer and top electrode 7
PV device testing 8
Charge extraction technique 8
Results and discussion 8
X-ray photoelectron spectroscopy analysis 8
Charge extraction and electron transport analysis 10
PV characterization 11
Application of newly developed Rb containg quadruple cation perovskite with Li-doped TiO_2 for high device Voc 12
Conclusion and future work 15
References 16

Funded by the Horizon 2020 Framework Programme of the European Union

Deliverable description

This public deliverable addresses the task to modify the TiO_2 scaffold by doping the oxide or deposit thin overlayers that will electronically passivate the TiO_2 surface removing trapping states. As a result the open circuit photo-voltage V_{OC} of the perovskite photovoltaic should be increased to at least 1.15 V.

Summary

Perovskite solar cells are one of the most promising photovoltaic technologies with their extraordinary progress in efficiency and the simple processes required to produce them. However, the frequent presence of a pronounced hysteresis in the current voltage characteristic of these devices arises concerns on the intrinsic stability of organo-metal halides, challenging the reliability of technology itself.

In order to progress further, and within GOTSolar project, the authors show that n-doping of mesoporous TiO_2 is possible by facile post-treatment of the films with lithium salts. The authors demonstrate that the Li-doped TiO_2 electrodes exhibit superior electronic properties, by reducing electronic trap states enabling faster electron transport. Perovskite solar cells prepared using the Li-doped TiO_2 films as scaffold to host the $CH_3NH_3PbI_3$ light harvester to produce substantially higher performances compared with undoped electrodes, improving the power conversion efficiency from 17 % to over 19 % with negligible hysteretic behaviour (lower than 0.3 %). As a result, the open circuit photo-voltage (V_{OC}) of the perovskite photovoltaic was increased to 1.118 V. Furthermore, for higher driving currents, Li-doped TiO_2 scaffolds were sensitized with newly developed perovskite light absorber such as rubidium cation doped perovskites (RbCsMAFA) to achieve outstanding *V*oc of 1.24 V.

ZnO synthesis and characterization as electron transfer layer was developed within GOTSolar project. The influence of the TiO_2 nanoparticle size influence on the PSC device performance is a background knowledge as well as Li-doped TiO_2. However, this metal oxide scaffold was applied in combination with quadruple cation perovskite light absorber to achieve V_{oc} higher than 1.15 V during the GOTSolar project.

Funded by the Horizon 2020 Framework Programme of the European Union

Introduction

Perovskite-based solar cells (PSCs) have made impressive strides in just a few years with maximum power conversion efficiencies (PCEs) jumping from 3.8 % [1] in 2009 to 22.1 % [2] in 2015. However, the frequent presence of a pronounced hysteresis in the current voltage characteristic of these devices arises concerns on the intrinsic stability of organo-metal halides, challenging the reliability of technology itself. Thus, further improvements are still expected, such rapid progress is unprecedented for any photovoltaic (PV) material. [3]

Mesoporous TiO_2 has been widely used for high-surface-area electrodes, in optoelectronic applications [4] and, in particular, in dye-sensitized solar cells (DSSCs)[5], where they have been demonstrated to collect and transport electrons photo injected from a surface adsorbed sensitizer. One strategy to improve DSSCs was to enhance the electron transport of the mesoporous TiO_2 making use of substitutional dopants [6,7]. Also, lithium intercalation has been employed to lower the conduction band edge of TiO_2 facilitating electron injection and transport in the mesoporous TiO_2. [8]

Therefore, it may be expected that the introduction of n-dopants would also enhance the performance of PSCs. However, so far very few studies have examined the doping effect on the electron transport within the mesoporous TiO_2 scaffold employed as PCSs. [9] This may be attributed to the perovskites already being excellent charge transporting materials inherently suited for electron conduction in high-efficiency solar cells.[10] This makes it challenging to investigate the effects of enhanced charge transport in mesoporous TiO_2 as this improvement would only have a discernible impact.

Materials and methods

Substrate preparation and Li-doping TiO_2

Nippon Sheet Glass of 10 Ωsq^{-1} was cleaned by sonication in 2 % Hellmanex water solution for 30 min. After rinsing with deionized water and ethanol, the substrates were further cleaned with ultraviolet ozone treatment for 15 min. Then, 30-nm TiO_2 compact layer was deposited on FTO via spray pyrolysis at 450°C from a precursor solution of titanium diisopropoxide bis(acetylacetonate) in anhydrous ethanol. After the spraying, the substrates were left at 450°C for 45 min and left to cool down to room temperature. Then, mesoporous TiO_2 layer was deposited by spin coating for 20 s at 4,000 r.p.m. with a ramp of 2,000 r.p.m. s^{-1}, using 30 nm particle paste (Dyesol 30 NR-D) diluted in ethanol to achieve 150- to 200-nm-thick layer. After the spin coating, the substrates were immediately dried at 100°C for 10 min and then sintered again at 450°C for 30 min under dry air flow. Li-doping of mesoporous TiO_2 was accomplished by spin coating a 0.1 M solution of Li-TFSI in acetonitrile. The solution was prepared freshly before the application in nitrogen atmosphere. 150 ml were poured on 1.4 x 2.4 cm^2 substrate. After 5 s of loading time, the spinning programme started with an acceleration of 1,000 r.p.m. to a final speed of 3,000 r.p.m., the substrate was left spinning for 30 s. Both Li+-doped and undoped electrodes were completed with a secondo calcination step at 450°C for 30 min. After cooling down to 150 °C, the substrates were immediately transferred in a nitrogen atmosphere glove box for the deposition of the perovskite films.

DSSC preparation procedure

Glass substrates for solid-state DSSCs were prepared following the same procedure used for PSC. 900 nm of mesoporous TiO_2 (Dyesol 30 nrd ethanol diluited) were deposited by spin coating at 4,000 r.p.m. After sintering, the substrates were cooled down to 70 °C and immersed in 0.1 mM solution of dye (Y123) in 1:1 mixture of acetonitrile and *tert*-butyl alcohol for 30 min. After the dyed films were rinsed in abundant acetonitrile, the hole conductor was applied by spin coating at 2,000 r.p.m. for 20 s. The hole transport composition and the following steps to complete the DSSCs were identical to what used for PSCs.

Perovskite precursor solution and film preparation

The perovskite films were deposited from a precursor solution containing FAI (1 M), PbI_2 (1.1 M), MABr (0.2 M) and $PbBr_2$ (0.2 M) in anhydrous dimethylformamide/ dimethylsulphoxide (4:1 (v:v)) solution. The perovskite solution was spin coated in a two-step programme at 1,000 and 4,000 r.p.m. for 10 s and 30 s, respectively. During the second step, 100 ml of chlorobenzene was poured on the spinning substrate 15 s prior the end of the programme. The substrates were then annealed at 100 °C for 1 h in nitrogen-filled glove box. We note that the perovskite precursor solution was prepared with a different composition from what reported by Jeon *et al.*, who used an equimolar amount of FAI and PbI_2 to achieve a certified PCE of 17.9 % with the mixed halide and cation formulation, $(FAPbI_3)_{0.85}(MAPbBr_3)_{0.15}$. Interestingly, systematic improvement in PCE was observed by moving away from the equimolar concentration for FAI and PbI_2 towards 10 mol % lower stoichiometric amount of FAI.

Perovskite precursor solution for quadruple cation perovskite

The organic cation iodide salts were purchased from Dyesol; the lead compounds from TCI and the CsI and RbI from abcr GmbH. The following formulations were composed by mixing appropriate amounts of FAI, MAI, CsI, RbI, PbI_2, MABr and $PbBr_2$.

Rb perovskite

$RbPbI_3$ was prepared from a precursor solution containing 1.2 M RbI and 1.3 M PbI_2 in anhydrous DMF:DMSO 4:1 (v:v).

Cs perovskite

$CsPbI_3$ was prepared from a precursor solution containing 1.2 M CsI and 1.3 M PbI_2 in anhydrous DMF:DMSO 4:1 (v:v).

MA/FA perovskite

The "mixed" perovskite precursor solutions were deposited from a precursor solution containing FAI (1 M), PbI_2 (1.1 M), MABr (0.2 M) and $PbBr_2$ (0.22 M) in anhydrous DMF:DMSO 4:1 (v:v).

Cs/FA perovskite

3 perovskite solutions were mixed; $CsPbI_3$ (containing 1.2 M CsI and 1.3 M PbI_2 in anhydrous DMF:DMSO 4:1 (v:v)); $FAPbI_3$ (containing 1.2 M FAI, 1.3 M PbI_2 in anhydrous DMF:DMSO 4:1 (v:v)); and $FAPbBr_3$ (containing 1.2 M FAI and 1.3 M $FABr_2$ in anhydrous DMF:DMSO 4:1 (v:v)). Then the 3 solutions are mixed to obtain the desired composition.

Rb/FA perovskite

3 perovskite solutions were mixed; $RbPbI_3$ (containing 1.2 M RbI and 1.3 M PbI_2 in anhydrous DMF:DMSO 4:1 (v:v)); $FAPbI_3$ (containing 1.2 M FAI, 1.3 M PbI_2 in anhydrous DMF:DMSO 4:1 (v:v)); and $FAPbBr_3$ (containing 1.2 M FABr and 1.3 M $PbBr_2$ in anhydrous DMF:DMSO 4:1 (v:v)). Then the 3 solutions are mixed to obtain the desired composition.

Cs/MA/FA perovskite

Then CsI, predissolved as a 1.5 M stock solution in DMSO, was added to the mixed perovskite (MA/FA) precursor to achieve the desired triple cation composition.

Rb/MA/FA perovskite

This follows the same procedure as Cs/FA/MA except RbI was added instead of CsI. RbI was predissolved as a 1.5 M stock solution in DMF:DMSO 4:1 (v:v).

Rb/Cs/FA perovskite

4 perovskite solutions were mixed: $CsPbI_3$ (containing 1.2 M CsI and 1.3 M PbI_2 in anhydrous DMF:DMSO 4:1 (v:v)); $RbPbI_3$ (containing 1.2 M RbI and 1.3 M PbI_2 in anhydrous DMF:DMSO 4:1 (v:v)); $FAPbI_3$ (containing 1.2 M FAI, 1.3 M PbI_2 in anhydrous DMF:DMSO 4:1 (v:v)); and $FAPbBr_3$ (containing 1.2 M FABr and 1.3 M $PbBr_2$ in anhydrous DMF:DMSO 4:1 (v:v)). Then the 4 solutions were mixed to obtain the desired composition.

Rb/Cs/MA/FA perovskite

RbI, predissolved as a 1.5 M stock solution in DMF:DMSO 4:1 (v:v), was added to the Cs/FA/MA triple cation perovskite to achieve the desired quadruple composition.

We prepare Rb compounds using the antisolvent approach developed recently for CsMAFA triple perovskite. In that work, we abbreviated "$Cs_x(MA_{0.17}FA_{0.83})_{(100-x)}Pb(I_{0.83}Br_{0.17})_3$" for convenience as Cs_xM (x is in percentage), where M stands for "mixed perovskite". i.e. Cs_0M means no Cs, is the basic composition our state-of-the-art devices. We note that these compositions refer to the precursor that also contains a lead excess as reported elsewhere. Including Rb complicates a convenient way of writing down these compounds.

We chose the following conventions (denoting only the precursor solutions).

For double perovskites and triple perovskites that contain Rb and Cs at the same time, we use stoichiometric ratios of the corresponding $RbPbI_3$ and $CsPbI_3$ perovskites instead of simply adding the salts.

The optimum $Cs_xFA_{(100-x)}$ ratio was reached at $Cs_{15}FA_{85}$ which we call CsFA from here. The optimum for $Rb_xFA_{(100-x)}$ was reached for $Rb_{10}FA_{90}$ which we call RbFA. The optimum $Rb_xCs_yFA_{(100-x-y)}$ composition was reached at $Rb_5Cs_{10}FA_{85}$ which we call RbCsFA.

The triple perovskites that contain both MA and FA are labelled according to the Cs_xM formalism but we now write Cs_xMAFA instead of Cs_xM. Rb then simply replaces Cs, i.e. Rb_xMAFA is the analogous triple perovskite to Cs_xMAFA. Optimization of the CsMAFA and RbMAFA. The optimum Rb concentration for Rb_xMAFA was reached at Rb_5MAFA. For the quadruple compounds, we chose to add the RbI to the Cs_5M triple. We use the same formalism as above and label the new series as $Rb_x(Cs_5M)_{(100-x)}$. Finally, the best performing devices were recorded at x=5 which we subsequently call RbCsMAFA throughout the report.

Hole transporting layer and top electrode

After the perovskite annealing, the substrates were cooled down for few minutes and a spirofluorene-linked methoxy triphenylamines (spiro-OMeTAD, from Merck) solution (70 mM in chlorobenzene) was spun at 4,000 r.p.m. for 20 s. The spiro-OMeTAD was doped with bis(trifluoromethylsulfonyl)imide lithium salt (Li-TFSI, from Aldrich), tris(2-(1H-pyrazol-1-yl)-4-tert-butylpyridine)-cobalt(III) tris(bis(trifluoromethylsulfonyl)imide) (FK209, from Dyenamo) and 4-tert-Butylpyridine (TBP, from Aldrich). The molar ratio of additives for spiro-OMeTAD was: 0.5, 0.03 and 3.3 for Li-TFSI, FK209 and TBP, respectively. Finally, 70–80nm of gold top electrode was thermally evaporated under high vacuum.

PV device testing

The solar cells were measured using a 450-W xenon light source (Oriel). The spectral mismatch between AM1.5G and the simulated illumination was reduced by the use of a Schott K113 Tempax filter (Präzisions Glas & Optik GmbH). The light intensity was calibrated with a Si photodiode equipped with an IR-cutoff filter (KG3, Schott) and it was recorded during each measurement. Current–voltage characteristics of the cells were obtained by applying an external voltage bias while measuring the current response with a digital source meter (Keithley 2400). The voltage scan rate was 10 mVs^{-1} and no device preconditioning was applied before starting the measurement, such as light soaking or forward voltage bias applied for long time. The starting voltage was determined as the potential at which the cells furnishes 1mA in forward bias, no equilibration time was used. The cells were masked with a black metal mask (0.16 cm^2) to estimate the active area and reduce the influence of the scattered light. The devices were characterized 2 days after their preparation.

Charge extraction technique

Charge extraction measurement were performer with Autolab potentiostat PGSTAT30 driven by NOVA software. The procedure for the charge extraction comprised four steps. First, the cell was kept for 10 s in dark at short circuit. At this stage, the carriers eventually accumulated in the intrinsic capacitances of the device were discharged. Then, the potential was brought to open circuit and the light was switched on for an equilibration time of 10 s. The light was then switched off and the open circuit voltage decay was monitored for a defined decay time T_d. In the last step, the cell was brought back to short circuit condition from V_{TD} (voltage at time T_d) and the discharge current was measured. The integration over the time (starting from *T*d) of this current gave the value of charge stored at the voltage V_{TD}.

Results and discussion

In the experimental study we applied the lithium ion surface treatment of the meso-porous TiO_2 layer via spin coating of a LiTFSI solution (see the Methods section). After the deposition and solvent evaporation, the substrates were sintered at 450 °C for 30 min. The introduction of Li^+ ions by the thermal diffusion modifies the surface of the particles. Together with the doping effect of the TiO_2 an overlayer of LiO_2 or LiOH could be formed. [11] Interestingly, also the formation of spinel structures like $Li_4Ti_5O_{12}$ was observed with a synthetic procedure similar to the one employed here. [12]

X-ray photoelectron spectroscopy analysis

We used X-ray photoelectron spectroscopy (XPS) to study the elemental composition of the Li-treated and untreated TiO_2 after sintering. No traces of sulphur or fluorine from the LiTFSI precursor for the treated sample were detected and the high resolution spectra for C 1s showed no difference between the Li-treated and untreated samples as seen in Supplementary Fig. 1.

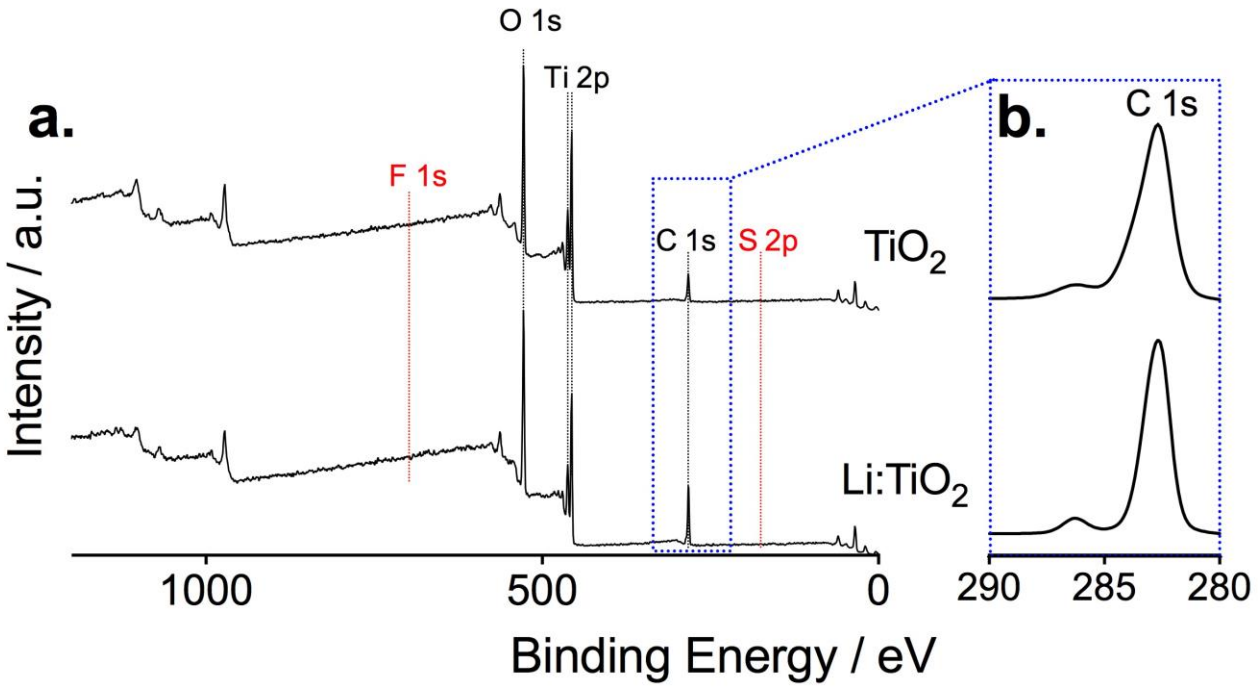

Figure 1.a) XPS survey spectra of Li-doped and undoped TiO_2 electrodes showing Ti 2p, O 1s and C 1s peaks. The lines in red depict the position of elements that are not present in the XPS spectrum but that are present in the precursor solution of LiTFSI b) high resolution spectra for C 1s for doped and undoped TiO_2.

The O 1s spectra in Fig. 2a,c show that Li-treated TiO_2 (Fig. 2a) has a more pronounced shoulder at the higher energy of the main peak compared with the untreated TiO_2 (Fig. 2c). The deconvolution of this signal reveals a second small peak at 531.2 eV for the untreated sample and a much more pronounced one for the Li-treated one that has been previously assigned to the oxygen interaction with the lithium [11].

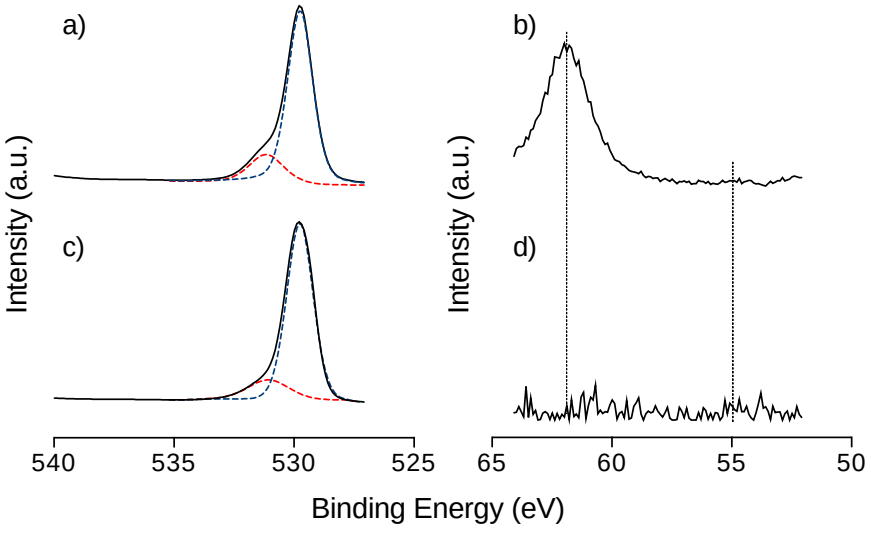

Figure 2. Doped and undoped mesoporous TiO_2 layers for the O 1s peaks Li doped (a) and the undoped control (c), Ti 3s and Li 1s peaks slightly visible at 55 eV for Li-doped (b) and the signal for the undoped TiO_2 here shown as reference, which reveals the absence of the peaks related to Ti 3s (dashed line at 61.5 eV) and Li 1s (d), dashed line at 54.9 eV.

The Ti 2p spectra (Fig. 3) shows that no difference was detected for the treated and untreated samples. On the right hand side of Fig. 2, the spectrum from 50 eV to 65 eV for the Li-treated TiO_2 (Fig.

2b) electrodes shows a peak corresponding to the Ti 3s and a weak, but distinct, signal for Li 1s. In the untreated TiO_2 (Fig. 2d), no such signals, measured over a series of samples, could be detected in this energy region and it is here shown as noise. The Ti 3s peak at 61.5 eV reveals the presence of Ti^{3+} for Li-treated electrodes and thus indicates that the Li^+ treatment induces a partial reduction of Ti^{4+} to Ti^{3+} within the TiO_2 lattice [13], which is not seen for the untreated electrode. Pathak *et al*. demonstrated that a small number of species with valency +3 can passivate the electronic defects or trap states that originate from oxygen vacancies within the TiO_2 lattice [7]. Accordingly, the Li+ doping mechanism is consistent with a passivation of electronic trap states resulting in improved charge transport properties and thus in better performing mesoporous TiO_2 electrodes. [14]

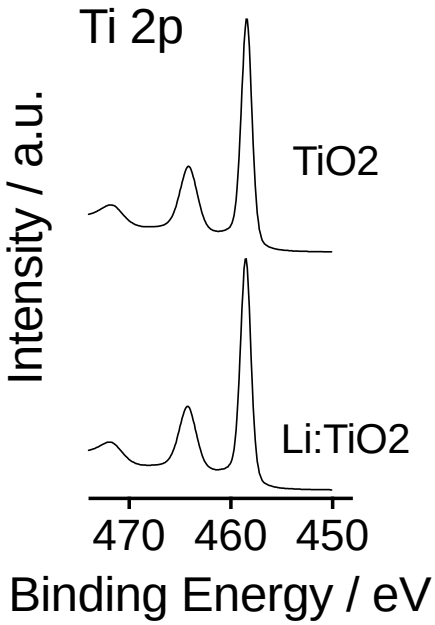

Figure 3. XPS Ti 2p spectra of Li-doped and undoped TiO_2 electrodes

Charge extraction and electron transport analysis

To study the impact of the lithium doping on the electronic states and the charge transport within the TiO_2, we prepared solid-state DSSCs using Li^+-doped mesoporous TiO_2 as electron transporting layer. DSSCs were prepared according to the previously reported procedures. [15]

In the DSSC field, charge extraction is a well-established light assisted technique, which qualitatively draws the density of state distribution below the TiO_2 conduction band. In Figure 4a, we report the charge extracted from the DSSCs at open circuit condition as a function of the open circuit voltage. At the same open circuit voltage, the devices employing Li:TiO_2 hold significantly less charges than the undoped TiO_2 (for example at 0.46 V, Li:TiO_2 and undoped TiO_2 holds 44.3 nC and 154.3 nC, respectively). This suggests that the Li^+ doping reduces the concentration of sub bandgap states in the TiO_2 supporting our previous conjecture that a partial reduction of Ti^{4+} to Ti^{3+} passivates the trapping states associated with oxygen vacancies within the TiO_2 lattice.

From the same DSSCs we extracted the charge transport time constant by intensity-modulated photocurrent spectroscopy. The cell was biased at short circuit under light and the time constants were measured for different light intensities. In Figure 4b, we compare the transport time constants for DSSCs

prepared with Li^+-treated and untreated TiO_2 electrodes. Li^+-treated devices display up to over one order of magnitude faster charge transport than the untreated devices over the whole range of current densities. To explain this trend, we note that charge transport in DSSCs is controlled by the electron transport in the TiO_2. In particular, it has been shown that the electronic transport in the TiO_2 is limited by the temporary localization of electrons within sub bandgap states, which can be passivated with different doping mechanisms. Our results indicate that Li^+ doping also reduces the concentration of sub bandgap states (Figure 4a) and improves the electronic transport within mesoporous TiO_2 electrodes (Figure 4b). Since we observe the presence of Li^+ ions within the TiO_2 lattice (Figure 2), we can regard this method as an effective way of n-doping *via* a facile post treatment of the mesoporous TiO_2 films. Even though such doping strategies may be effective for improving DSSC performance, they may not necessarily benefit PSCs, since the latter already accomplish fast charge transport within the perovskite layer.

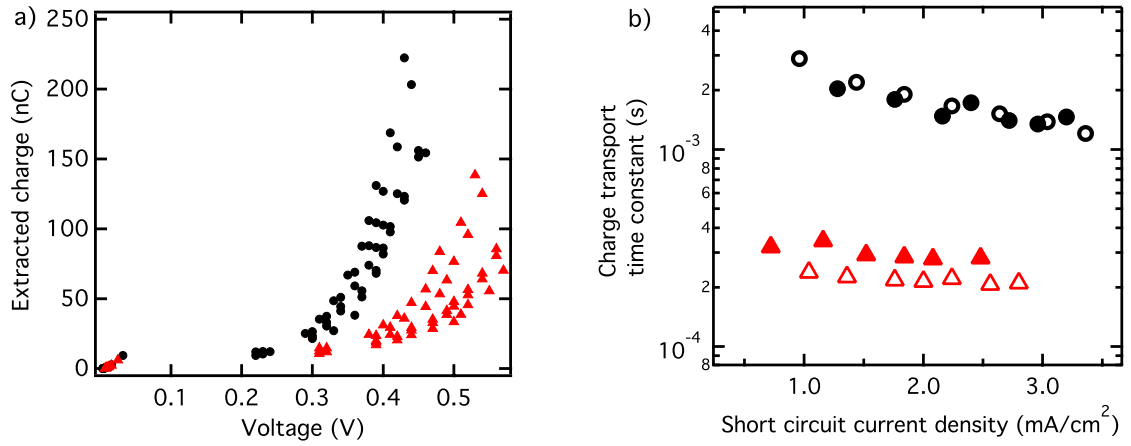

Figure 4. (a) Charge extracted at open circuit as function of the voltage for no treated samples (*black*) and Li-doped samples (*red*) and (b) charge transport lifetime as function of the short circuit current density for solid-state dye-sensitized solar cells prepared without and with Li-doped mesoporous TiO_2 (*black* and *red* markers respectively, open and closed symbols refer to different samples).

PV characterization

Figure 5 shows a typical current density-voltage (JV) characteristic that we measured for PSCs with and without Li^+-doped mesoporous TiO_2. In Table 1, we summarize the device performance parameters, as extracted from the J-V curves in Figure 5, and the light intensity measured during each JV scan. We note that the difference between the backward and the forward scans is significantly larger in the control than in the Li^+-doped device. The short circuit currents are quite similar, while the Li^+-doped device showed significantly larger open circuit voltage (about 60mV) and 0.11 units higher fill factor. The current mismatch between the measured current density and the current density calculated by the IPCE over the Solar AM1.5 G spectrum was less than 2 %. The overall power conversion efficiency of devices employing the Li^+-doped TiO_2 electrodes was systematically higher than the devices employing the undoped scaffold. This result is consistent with the fact that the Li^+-doping decreases the number of deep traps, which act as recombination centers and induces faster charge transport within the TiO_2, improving the open circuit voltage and fill factor respectively.

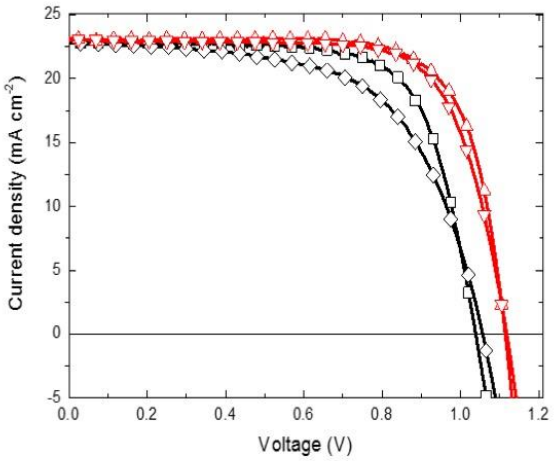

Figure 5. Current density-voltage curves of the solar cells with and without the Li^+ doping (red and black curve respectively) collected under AM1.5 simulated sun light. Devices were masked with a black metal aperture of 0.16 cm^2 to define the active area. The curves were recorded scanning at 0.01 V s^{-1} from forward bias to short circuit condition and *vice versa* with no device preconditioning such as light soaking or holding at forward voltage bias. Legend: ◇ control forward scan □ control reverse scan ▽ Li+ doped forward scan △ Li+ doped reverse scan.

Table 1. Solar cell performance parameters: short circuit photocurrent (J_{sc}), power conversion efficiency (PCE), open circuit voltage (V_{oc}), fill factor (FF) extracted from the data in Figure 5.

	Scan direction	J_{sc} (mA cm^{-2})	V_{oc} (V)	FF	PCE (%)	Light intensity (mW cm^{-2})
Li^+ doped	backward	23.0	1.114	0.74	19.3	98.1
	forward	23.1	1.118	0.72	19.0	
control	backward	22.7	1.038	0.72	17.1	99.4
	forward	22.7	1.056	0.61	14.7	

Application of newly developed Rb containg quadruple cation perovskite with Li-doped TiO_2 for high device Voc

We applied this outstanding Li-doped TiO_2 scaffolds with recently developed Rb-containing perovskite materials (Figure 6) as light absorber.

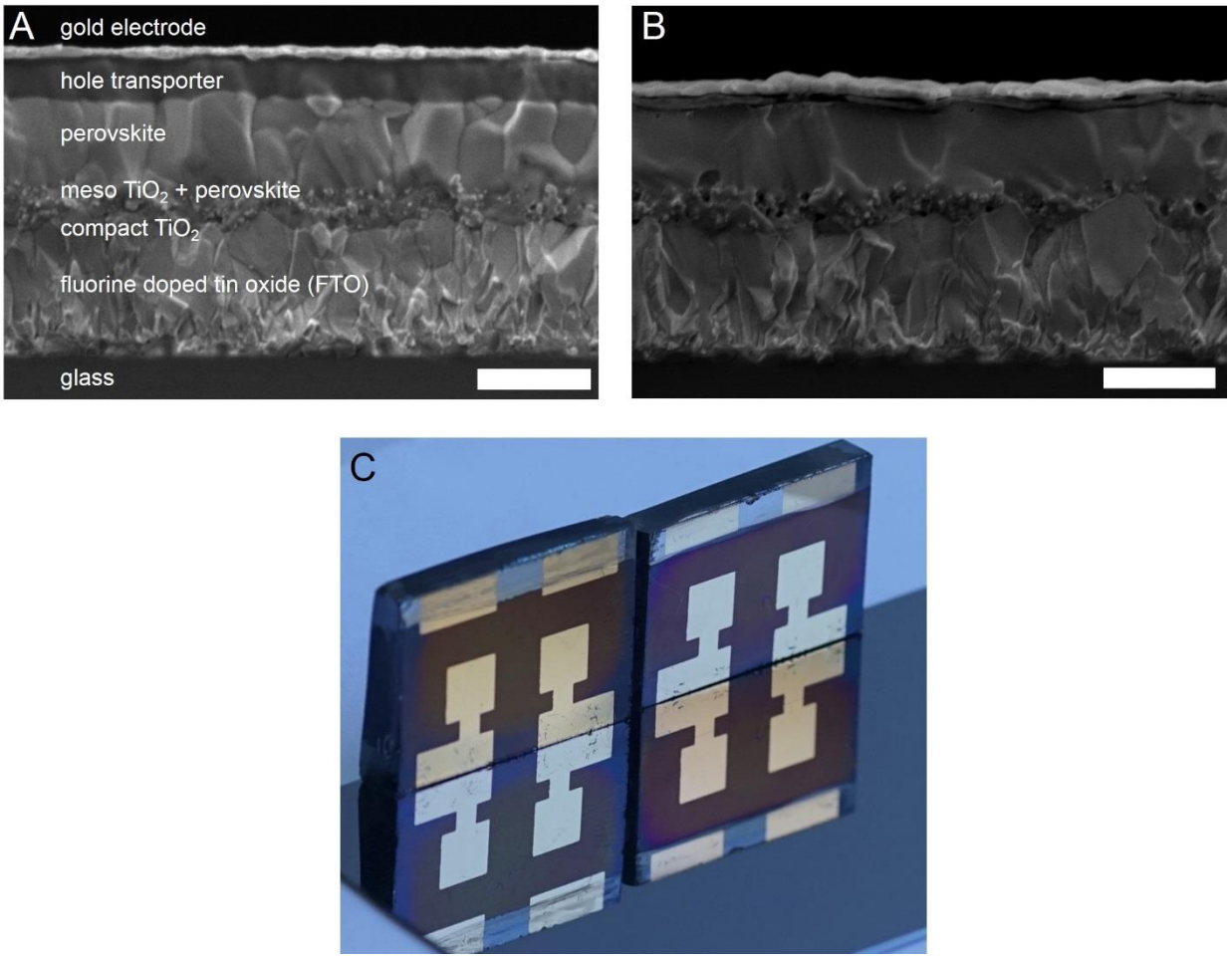

Figure 6. Cross sectional scanning electron microscope (SEM) images of an RbCsMAFA perovskite solar cell with the hole transporter material (A) spiro-OMeTAD (thickness 200-250 nm) and (B) PTAA (thickness 30-50 nm). The scale bars are 500 nm. (C) Image of typical devices.

Remarkably for RbCsMAFA devices, the average open-circuit voltage (V_{oc}) is increased from 1.120 to 1.158 V and the fill factor from 0.75 to 0.78. In Figure 7, we show the RbCsMAFA champion cell reached a stabilized power output of 21.6 % with a fill factor of 81 % and 1.180 V open-circuit voltage.

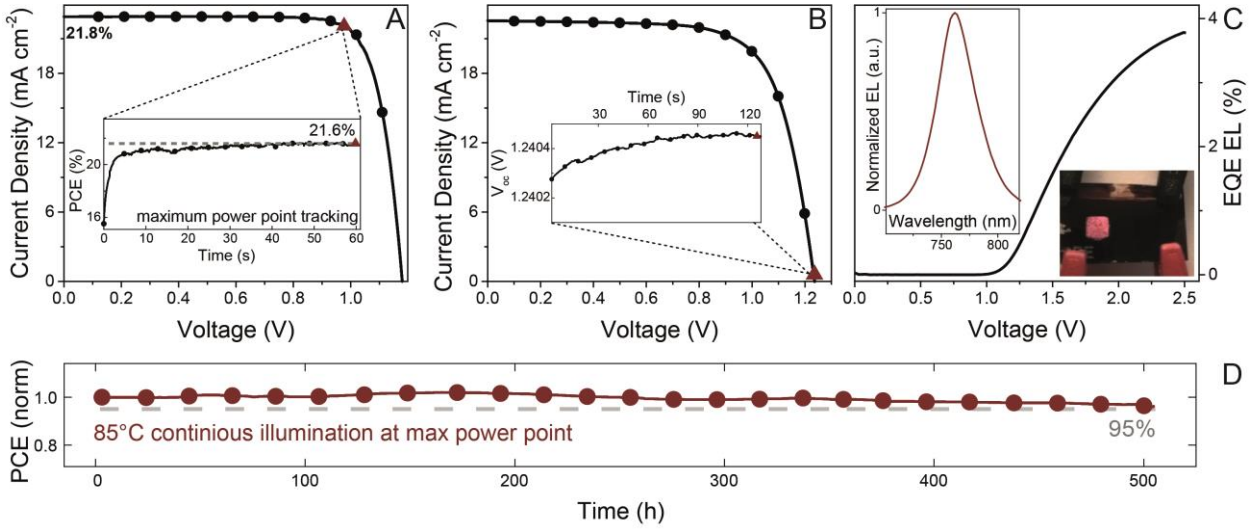

Figure 7. Champion efficiency, open-circuit voltage, electroluminescence and high temperature stability.

To correctly determine the V_{oc}, we investigated RbCsMAFA devices with the active area being fully illuminated, held at room temperature, and under an inert nitrogen atmosphere. This setup permitted an accurate V_{oc} value without heating or degradation effects (from moisture for example). In Figure 7B, for one of our highest performing devices, we measured an outstanding V_{oc} of 1.240 V confirmed by the inset that is tracking the V_{oc} over time. The "loss-in-potential" (difference between V_{oc} and band gap) is only ~0.39 V, which is one of the lowest recorded for any PV material, implying very small non-radiation recombination losses. [16] The high V_{oc} is particularly intriguing because this is the major parameter preventing PSCs from reaching their thermodynamic limit (J_{sc} and FF are already approaching their maximal values).

Despite the high efficiencies and an outstanding EL (Figure 7C), this Rb-containing perovskite material must be able achieve high stability. For the combined heat-light stress tests in this work, we find a thin layer of PTAA is used as HTM. We aged devices for 500 hours at 85 °C under continuous illumination with full solar intensity and maximum power point tracking in a nitrogen atmosphere. This compounded stress test exceeds industrial standards [17]. We show the result in Figure 7D (red curve, circles). The device started with > 17 % efficiency at room temperature before the aging protocol was applied. During the 85 °C step (in which the V_{oc} is inevitably lowered), the device retained 95 % of its initial performance.

Conclusion and future work

In summary, we demonstrated a doping mechanism that allowed preparing mesoporous TiO_2 electrodes with superior electron properties. The doping can be accomplished with a facile post treatment of the mesoporous TiO_2 making use of lithium salts to induce a partial reduction of Ti^{4+} to Ti^{3}+ within the TiO_2 lattice and passivating electronic defect states acting as nonradiative recombination centres. Moreover, we exploit the Li+-doped mesoporous TiO_2 electrodes to improve the maximum power conversion efficiency of perovskite solar cells from 17% to over 19 %, which is comparable to the highest values reported in the literature. Finally, the Li+-doping decreases the number of deep traps, which act as recombination centres and induces faster charge transport within the TiO_2, improving the open circuit photo-voltage V_{OC} to 1.118 V. Furthermore, for higher driving currents, Li-doped TiO_2 scaffolds were applied with newly developed perovskite light absorbers such as rubidium cation doped perovskites (RbCsMAFA) to achieve outstanding *V*oc of 1.24 V. $SrTiO_3$ and $MgTiO_3$ Core-shell scaffold studies were performed as passivating layers on top of Li-doped TiO_2 films. The surface of TiO_2 particles were treated with hydroiodic acid to prepare iodide doped titania (I-TiO_2) films to apply in PSC devices.

The future work will be focused on development of alternative oxide materials such as SnO_2, Zn_2SnO_4, $SrTiO_3$ and $BaSnO_3$ that can act as electron selective contacts.

References

[1] Kojima, A., Teshima, K., Shirai, Y. & Miyasaka, T. Organometal hali de perovskites as visible-light sensitizers for photovoltaic cells. J. Am. Chem. Soc. 131, 6050–6051 (2009).
[2] NREl, Research Cell Efficiency Records. 2016.
[3] Park, N. G. Perovskite solar cells:an emerging photovoltaic technology. Mater. Today 18, 65–72 (2015).
[4] Crossland, E. J. W. et al. Mesoporous TiO_2 single crystals delivering enhanced mobility and optoelectronic device performance. Nature 495, 215–219 (2013).
[5] O'Regan, B. & Gratzel, M. A low-cost, high-efficiency solar cell based on dyesensitized colloidal TiO_2 films. Nature 353, 737–740 (1991).
[6] (a) Ko, K. H., Lee, Y. C. & Jung, Y. J. Enhanced efficiency of dye-sensitized TiO2 solar cells (DSSC) by doping of metal ions. J. Colloid Interface Sci. 283, 482–487 (2005); (b) Fabregat-Santiago, F. et al. High carrier density and capacitance in TiO_2 nanotube arrays induced by electrochemical doping. J. Am. Chem. Soc. 130, 11312–11316 (2008); (c) Lee, S. et al. Nb-doped TiO_2: a new compact layer material for TiO2 dyesensitized solar cells. J. Phys. Chem. C 113, 6878–6882 (2009); (d) Lü, X. et al. Improved-performance dye-sensitized solar cells using Nb-doped TiO2 electrodes: efficient electron injection and transfer. Adv. Funct. Mater. 20, 509–515 (2010); (e) Nah, Y. C., Paramasivam, I. & Schmuki, P. Doped TiO2 and TiO2 nanotubes: synthesis and applications. Chemphyschem. 11, 2698–2713 (2010); (f) Zhang, X., Liu, F., Huang, Q.-L., Zhou, G. & Wang, Z.-S. Dye-sensitized W-doped TiO_2 solar cells with a tunable conduction band and suppressed charge recombination. J. Phys. Chem. C 115, 12665–12671 (2011); (g) Zhang, X., Wang, S.-T. & Wang, Z.-S. Effect of metal-doping in TiO2 on fill factor of dye-sensitized solar cells. Appl. Phys. Lett. 99, 113503 (2011); (h) Duan, Y. et al. Sn-doped TiO_2 photoanode for dye-sensitized solar cells. J. Phys. Chem. C 116, 8888–8893 (2012); (i) Cho, I. S. et al. Codoping titanium dioxide nanowires with tungsten and carbon for enhanced photoelectrochemical performance. Nat. Commun. 4, 1723
(2013); (h) Leijtens, T. et al. Overcoming ultraviolet light instability of sensitized TiO_2 with meso-superstructured organometal tri-halide perovskite solar cells. Nat. Commun. 4, 2885 (2013).
[7] Pathak, S. K. et al. Performance and stability enhancement of dye-sensitized
and Perovskite solar cells by Al doping of TiO_2. Adv. Funct Mater. 24,
6046–6055 (2014).
[8] (a) Kopidakis, N., Benkstein, K. D., van de Lagemaat, J. & Frank, A. J. Transportlimited recombination of photocarriers in dye-sensitized nanocrystalline TiO_2 solar cells. J. Phys. Chem. B 107, 11307–11315 (2003); (b) Olson, C. L., Nelson, J. & Islam, M. S. Defect chemistry, surface structures, and lithium insertion in anatase TiO_2. J. Phys. Chem. B. 110, 9995–10001 (2006); (c) Abate, A. et al. Lithium salts as 'redox active' p-type dopants for organic semiconductors and their impact in solid-state dye-sensitized solar cells. Phys. Chem. Chem. Phys. 15, 2572–2579 (2013); (d) Abate, A. et al. Protic ionic liquids as p-dopant for organic hole transporting
materials and their application in high efficiency hybrid solar cells. J. Am. Chem. Soc. 135, 13538–13548 (2013).
[9] Kim, D. H. et al. Niobium doping effects on TiO_2 mesoscopic electron transport layer-based Perovskite solar cells. ChemSusChem 8, 2392–2398 (2015).
[10] Stranks, S. D. et al. Electron-hole diffusion lengths exceeding 1 micrometer in an organometal trihalide perovskite absorber. Science 342, 341–344 (2013).
[11] Södergren, S. et al. Lithium intercalation in nanoporous anatase TiO_2 studied with XPS. J. Phys. Chem. B 101, 3087–3090 (1997).

[12] Bouattour, S. et al. Li-doped nanosized TiO_2 powder with enhanced photocalatylic acivity under sunlight irradiation. Appl. Organomet. Chem. 24, 692–699 (2010).
[13] Olson, C. L., Nelson, J. & Islam, M. S. Defect chemistry, surface structures, and lithium insertion in anatase TiO_2. J. Phys. Chem. B. 110, 9995–10001 (2006).
[14] Cappel, U. B. et al. Characterization of the interface properties and processes in solid state dye-sensitized solar cells employing a perylene sensitizer. J. Phys. Chem. C 115, 4345–4358 (2011).
[15] Abate, A. et al. An organic 'Donor-Free' dye with enhanced open-circuit voltage in solid-state sensitized solar cells. Adv. Energy Mater. 4, 1400166 (2014).
[16] M. A. Green, Radiative efficiency of state-of-the-art photovoltaic cells. *Progress in Photovoltaics* **20**, 472 (2012).
[17] Y. G. Rong, L. F. Liu, A. Y. Mei, X. Li, H. W. Han, Beyond Efficiency: the Challenge of Stability in Mesoscopic Perovskite Solar Cells. *Advanced Energy Materials* 5, (Oct 21, 2015).